forum acusticum 2026
8-12 September · Graz, Austria

IN-SITU ESTIMATION OF SOUND ABSORPTION COEFFICIENTS AT GRAZING INCIDENCE WITH BOOSTLETS

Annika Strömhäll[1], Arif Onur Yürek[2], Tapio Lokki[2], Elias Zea[1]

[1] *The Marcus Wallenberg Laboratory for Sound and Vibration Research, Department of Engineering Mechanics, KTH Royal Institute of Technology, Stockholm, Sweden*
[2] *Department of Information and Communications Engineering, Aalto University, Espoo, Finland*

Abstract

Estimating angle-dependent sound absorption in situ requires separating incident and outgoing wavefields, which is difficult at grazing incidence because their arrivals overlap. We assess the boostlet transform for this task using a scanned one-dimensional microphone array. A measured space–time window is extrapolated by sparse boostlet synthesis, analysed into localized coefficients, and partitioned using translation and the known propagation geometry. Third-octave sound absorption follows from the reflected-to-direct energy ratio of boostlet coefficients. Tests used rigid and porous panels at nominal grazing angles of 8° and 30°. For the nominal 30° high-angle configuration, partial separation is obtained, but non-zero rigid-board absorption exposes systematic bias. JCAL predictions provide a qualitative material-model benchmark for this configuration, and wavenumber-based re-estimation gave an effective incidence angle of $\beta_{\text{eff}} = 30.68°$, rounded to 31° for the model. At 8°, the incident and reflected wavefronts occupy strongly overlapping boostlet support, and separation fails. Coefficient-support overlap and finite-aperture resolution are the dominant limitations, motivating array orientations that map the wavefronts to disjoint boostlet coefficient regions.

Keywords: *sound absorption, grazing incidence, microphone array, boostlets, wavefield separation*

1. Introduction

Standardized tube and reverberation-room measurements characterize normal- and random-incidence absorption, respectively, but neither directly resolves the dependence on incidence angle under the mounting conditions of a finite sample [1], [2]. In-situ approaches, therefore, infer the incident and reflected components from measurements close to the surface. Tamura's double-plane spatial-Fourier method separated upward- and downward-propagating content in wavenumber space [3], [4]; later approaches employed near-field holography, plane- or spherical-wave models, and regularized array inversion [5], [6], [7], [8], [9]. Their accuracy depends on the propagation model and on whether the aperture resolves the competing components. Near grazing incidence, the direct and reflected waves become difficult to distinguish, and, for finite samples, edge-diffraction and non-local reaction further complicate the interpretation [10], [11]

This study investigates an alternative representation based on boostlets: a set of localized functions parametrized by scale, hyperbolic rotation, and translation in space–time. The hyperbolic rotation preserves the geometry of the nondispersive wave equation, while localization allows individual wavefronts to be described with relatively few coefficients [12], [13]. This is attractive for finite, non-periodic measurement windows for which a global plane-wave expansion often spreads a localized arrival over many coefficients.

We ask whether incident and outgoing wavefields measured by a 1D array parallel to a sample can be represented by approximately disjoint boostlet coefficients, separated, and used to estimate third-octave absorption. Measurements of a rigid reference and a porous bioboard at nominal grazing angles of 8° and 30° are considered; the latter is referred to as the high-angle configuration. The contribution is twofold: a boostlet-domain post-processing chain is formulated, and its operating limitation is identified when wavefronts overlap in the translation coordinate.

Corresponding author: *arif.yurek@aalto.fi.*

2. Background

2.1. Sound absorption measurements

For the experimental validation of the proposed method, two materials were investigated: a rigid board and a bioboard (Lumir, Finland). While the bioboard is a bio-based sound-absorbing material manufactured using a cellulose-based foam-forming process, the earlier served as a rigid reference surface. Prior to the in-situ measurements, impedance-tube measurements were performed to characterize the bioboard and subsequently simulate its angle-specific sound absorption coefficients.

Three cylindrical specimens (29 mm diameter) were extracted from the bioboard and measured using a Brüel & Kjær Type 4206 impedance tube employing the three-microphone method [14]. In addition, the static air-flow resistivity (σ) was measured according to ISO 9053 [15]. The remaining Johnson–Champoux–Allard–Lafarge (JCAL) parameters, namely the porosity (ϕ), high-frequency limit of the dynamic tortuosity (α_∞), characteristic viscous length (Λ), characteristic thermal length (Λ'), and static thermal permeability (κ_0), were estimated from the impedance-tube measurements using RoKCell (Matelys, France) [16]. The parameter values were then averaged across the three specimens and used to simulate angle-dependent sound absorption coefficients in AlphaCell (Matelys, France) [17]. Anechoic end conditions were assumed to match the experimental configuration, in which the bioboard was mounted without a rigid backing.

2.2. Boostlet preliminaries

Let $\boldsymbol{\zeta} = (x, ct)^\mathsf{T}$ denote a dimensionally homogeneous space–time coordinate, where c is the speed of sound. From a mother function $\psi \in L^2(\mathbb{R}^2)$, a continuous boostlet is [12]

$$\psi_{a,\theta,\boldsymbol{\tau}}(\boldsymbol{\zeta}) = a^{-1}\psi\left(\mathbf{B}_\theta^{-1}\frac{\boldsymbol{\zeta}-\boldsymbol{\tau}}{a}\right), \quad \mathbf{B}_\theta = \begin{bmatrix} \cosh\theta & -\sinh\theta \\ -\sinh\theta & \cosh\theta \end{bmatrix}. \tag{1}$$

where $a > 0$ is the dilation, $\theta \in \mathbb{R}$ is the Lorentz-boost parameter, and $\boldsymbol{\tau} = (\tau_x, c\tau_t)^\mathsf{T}$ is a space–time translation. With the angular-frequency convention $\widehat{p}(k,\omega) = \iint p(x,t)e^{-\mathrm{i}(kx-\omega t)}\,\mathrm{d}x\,\mathrm{d}t$, the transformation preserves the hyperbolae $\omega^2 - c^2k^2 = \text{constant}$.

Dilation a selects a hyperbolic spectral interval, the boost parameter θ selects an apparent propagation direction, and translation τ localizes the atom along a wavefront. For a plane wave observed along the array, $\tanh\theta = ck_x/\omega$. If β is measured from the sample surface, $k_x = (\omega/c)\cos\beta$ and therefore $\tanh\theta = \cos\beta$.

In the implementation, a, θ, and $\boldsymbol{\tau}$ are sampled using the tensor-Meyer construction in [12]. Let $\gamma = (j, n, \boldsymbol{\tau})$ collect scale, boost, and translation indices, $\mathcal{A}$ and $\mathcal{S}$ denote boostlet analysis and synthesis operators, and define $c_\gamma = (\mathcal{A}p)_\gamma = \langle p, \psi_\gamma\rangle$. The desired observation model is

$$\mathbf{y} \simeq \mathcal{P}_\Omega\mathcal{S}(\mathbf{c}_\mathrm{i} + \mathbf{c}_\mathrm{r} + \mathbf{c}_\mathrm{s}) + \mathbf{n}, \quad \Pi_q^\varepsilon = \mathrm{supp}_\varepsilon(\mathbf{c}_q). \tag{2}$$

where $\mathbf{y}$ contains the samples selected by the aperture/window operator $\mathcal{P}_\Omega$; $q \in \{\mathrm{i},\mathrm{r},\mathrm{s}\}$ denotes incident, specularly reflected, and other scattered content; $\mathbf{n}$ contains noise and model error; and $\mathrm{supp}_\varepsilon(\mathbf{c}_q) = \{\gamma : |c_{q,\gamma}| > \varepsilon\}$ is an effective boostlet support. The hypothesis being tested is that the components are concentrated on weakly overlapping regions, ideally $\Pi_q^\varepsilon \cap \Pi_{q'}^\varepsilon = \varnothing$ for $q \neq q'$. Exact support disjointness is not expected for a redundant, finite-bandwidth frame, nor do disjoint coefficient masks imply orthogonal reconstructed fields. The condition concerns fields that share a phase speed and frequency content, yet remain separable if their translation supports do not overlap.

3. Method and post-processing

3.1. Experimental setup

The in-situ measurements of the surface materials were conducted in the anechoic chamber at Aalto Acoustics Lab using the moving-microphone method. A rigid mounting frame was constructed to ensure accurate and repeatable positioning of the sound source, test samples, and microphone. A directional audio panel (Sound Shower Compact, Panphonics) with an aperture of 60×60 cm generated the sound field. Above approximately 571 Hz, the panel provides a close approximation to a plane-wave excitation within the measurement region.

For clarity, the experimental configuration is described using a presentation-oriented Cartesian coordinate system. The geometry and measured sound field are represented in a vertical reference plane ($y = 0$), corresponding to an x–z cross-section through the measurement region.

Two square test samples with identical surface dimensions of 68×68 cm were investigated in the experiments: a 2-cm-thick rigid board and a 3-cm-thick bioboard. Each sample was mounted vertically on an adjustable holder, with its surface coinciding with the plane $z = 0$. The grazing angle β is measured from the sample surface. The sound source was mounted vertically on a horizontal beam, allowing lateral translation to realize nominal grazing angles of $\beta = 8°$ and $30°$. Wavenumber-based re-estimation of the high-angle plane-wave incidence gave $\beta_\mathrm{eff} = 30.68°$, which was rounded to $\beta = 31°$ for the corresponding JCAL simulation. At each source position, the source panel was oriented towards the vertical centreline of the test sample. The microphone was positioned in front of the sample surface and translated within $y = 0$ using a two-dimensional motorized positioning system (ACRO 1010, OpenBuilds) that was placed behind the sample.

Signal playback and microphone acquisition were performed using a multi-channel audio interface (RME Fireface UFX+). The sound field was measured using a laboratory-grade microphone (GRAS 46AF) connected to a power module (GRAS 12AG). Signal generation, data acquisition, and scanner control were integrated into a MATLAB framework.

The measurement grid was a linear array within $y = 0$, positioned 15 cm in front of the sample surface. The microphone spacing along the x-axis was 1 cm. At

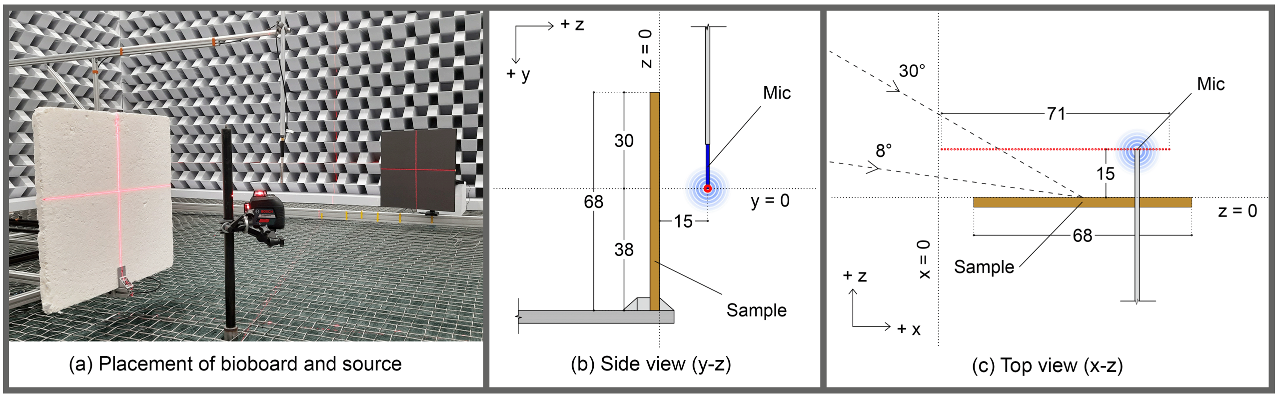

Figure 1: (a) Photograph of the experimental setup showing the mounted bioboard, moving microphone, and source placement for 8° grazing incidence. (b) Side-view technical drawing (y–z plane). (c) Top-view technical drawing (x–z plane) with grazing angles. Microphone positions are marked with red dots.

each receiver position, a logarithmic sine sweep covering 100–20 000 Hz was recorded to estimate the impulse responses (Fs = 192 kHz). Figure 1 presents a photograph together with front- and side-view drawings of the experimental configuration.

3.2. Signal processing with boostlets

3.2.1. Windowing and sparse extrapolation

For one microphone line, the measured pressure samples form a matrix $\mathbf{P} \in \mathbb{R}^{N_x \times N_t}$. The temporal axis is first resampled to $\widetilde{f}_s = c/\Delta x$ so that one temporal sample corresponds to the acoustic travel time over one spatial increment. A rectangular window extracts the incident and outgoing arrivals. Because the available spatial interval gives a truncated x–t window, the field is extrapolated to a 128×128 grid by solving

$$\mathbf{b}^{\star}_{\text{ext}} = \arg\min_{\mathbf{b}} \frac{1}{2}\|\mathcal{P}_{\Omega}\mathcal{S}\mathbf{b} - \mathbf{y}\|_2^2 + \mu\|\mathbf{b}\|_1. \quad (3)$$

Here $\mathcal{S}$ synthesizes a full grid from the sparse extrapolation coefficients $\mathbf{b}^{\text{ext}}$, $\mathcal{P}_{\Omega}$ retains the actually measured samples, and $\mu > 0$ balances measured-region fidelity and sparsity. Equation (3) is solved with FISTA [18], with μ selected via the L-curve. The extrapolated field is then $\widetilde{\mathbf{p}} = \mathcal{S}\mathbf{b}^{\star}_{\text{ext}}$. These sparse synthesis coefficients are conceptually distinct from the analysis maps used next.

3.2.2. Coefficient selection and wavefield partition

The analysis transform of $\widetilde{\mathbf{p}}$ produces a translation map for each discrete scale/boost atom,

$$\begin{aligned} c_{j,n}(\boldsymbol{\tau}) &= \langle \widetilde{p}, \psi_{j,n,\boldsymbol{\tau}} \rangle \\ &= \mathcal{F}^{-1}\left\{ \widetilde{P}\, \overline{\widehat{\psi}_{j,n}} \right\}(\boldsymbol{\tau}), \\ e_{j,n} &= \sum_{\boldsymbol{\tau}} |c_{j,n}(\boldsymbol{\tau})|^2. \end{aligned} \quad (4)$$

Thus, $c_{j,n}(\boldsymbol{\tau})$ is itself a correlation between the field and a translated atom. Peaks of $|c_{j,n}|$ locate matching wavefronts, and atoms whose energy $e_{j,n}$ exceeds a common threshold (derived heuristically from the bioboard reference configuration) are retained.

For the parallel geometry, the retained coefficient maps are divided by a line in translation space,

$$\begin{aligned} t_{\text{sep}}(\tau_x) &= t_0 + \frac{\cos\beta}{c}\tau_x + \Delta, \\ H_{\text{i}}(\boldsymbol{\tau}) &= \mathbb{1}[\tau_t \le t_{\text{sep}}(\tau_x)], \\ H_{\text{o}}(\boldsymbol{\tau}) &= 1 - H_{\text{i}}(\boldsymbol{\tau}). \end{aligned} \quad (5)$$

where t_0 aligns the expected direct arrival and Δ places the boundary between the two ridges. The incident and outgoing coefficient maps are $c_{j,n,\text{i}} = H_{\text{i}} c_{j,n}$ and $c_{j,n,\text{o}} = H_{\text{o}} c_{j,n}$, followed by dual-frame synthesis $\widehat{p}_q = \mathcal{S}_{\text{d}}\mathbf{c}_q$, $q \in \{\text{i}, \text{o}\}$. The offset Δ is geometry-informed but manually adjusted for each configuration.

3.2.3. Sound absorption estimation

Let $\widehat{P}_q(k,\omega)$ be the 2D Fourier transform of the separated field. Comparison with JCAL model requires bands of ordinary temporal frequency. For the mth third-octave band, $\omega_{m,-} = 2\pi f_m 2^{-1/6}$ and $\omega_{m,+} = 2\pi f_m 2^{1/6}$, and we define a hyperbolic third-octave band filter

$$F_m(k,\omega) = \mathbb{1}\left[\omega_{m,-} \le |\omega^2 - k^2| < \omega_{m,+}\right], \quad (6)$$

from which the energy is calculated for each field $q \in \{\text{i}, \text{o}\}$ as

$$E_{q,m} = \sum_{k,\omega} |F_m(k,\omega)\widehat{P}_q(k,\omega)|^2. \quad (7)$$

The absorption coefficient estimate is then

$$\alpha^{\star}(f_m) = 1 - \frac{E_{\text{o},m}}{E_{\text{i},m}}. \quad (8)$$

For a finite sample, this is an apparent absorption estimate: scattering not captured by the array appears as loss, whereas captured diffraction is assigned to the outgoing field, which reduces that apparent loss.

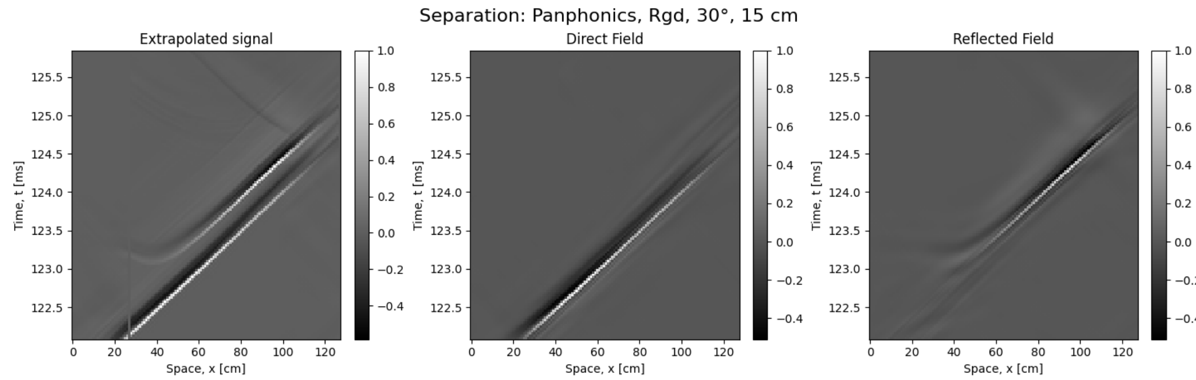

(a)

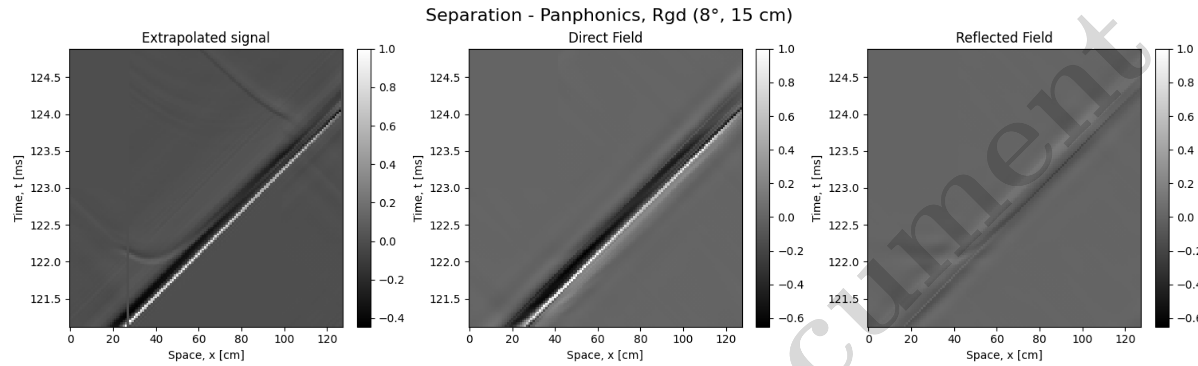

(b)

Figure 2: Synthesized space–time fields for the rigid board at 15 cm and nominal grazing angles of (a) 30° and (b) 8°. Each row shows the extrapolated total, incident, and outgoing fields. The original labels "Direct" and "Reflected" denote the latter two estimates. These are physical x–t fields, not coefficient maps; independent colour scales preclude amplitude comparison between rows.

4. Results and analysis

4.1. Wavefront separation

Figure 2 shows the result of synthesizing the extrapolated, direct, and reflected fields. The reconstruction successfully extends the dominant wavefronts across the padded spatial interval while preserving their slopes in the measured region. Energy is concentrated in a small subset of scale/boost atoms, consistent with the sparse representation expected for localized wavefronts. However, sparsity of the complete field does not by itself imply separability: several energetic coefficient maps contain both the incident and specular ridges (not shown here for brevity).

For the nominal 30° high-angle configuration, the two ridges are sufficiently separated over part of the translation plane for the geometric mask to produce recognizable incident and outgoing reconstructions. Comparison of the synthesized incident field with the free-field measurement nevertheless reveals residual reflected energy. At 8°, the wavefronts are closer and overlap over a larger portion of the window. The mask then divides energy belonging to a common ridge rather than selecting disjoint coefficient support, and leakage across direct and reflected fields increases markedly.

4.2. Absorption estimates and validation

Panel (a) of Fig. 3 uses the rigid board as a diagnostic of the incident–outgoing separation. Its physical absorption is expected to remain small over the frequency range in which transmission and finite-size effects are weak. The retrieved coefficient nevertheless departs markedly from zero, and the estimates for the two angles differ strongly. In particular, the 8° curve displays negative absorption at octave bands below 630 Hz. These results reveal a systematic bias in the wavefield-energy partition, which may also affect the bioboard estimates.

Panel (b) compares the boostlet-based bioboard estimates with the corresponding JCAL predictions. The nominal 30° measurement, for which the wavenumber-derived effective angle is $\beta_{\text{eff}} = 30.68°$, is compared with the JCAL calculation at $\beta = 31°$. Above the lowest bands, the measured and modelled curves are both high and nearly flat, giving broad qualitative agreement. At 8°, however, the estimate is generally higher once it enters the plotted range and does not reproduce the broad spectral minimum predicted by the model. This disagreement is consistent with the stronger incident–outgoing support overlap observed in Fig. 2.

The results in Fig. 3 should therefore at this stage be interpreted as a consistency benchmark for the

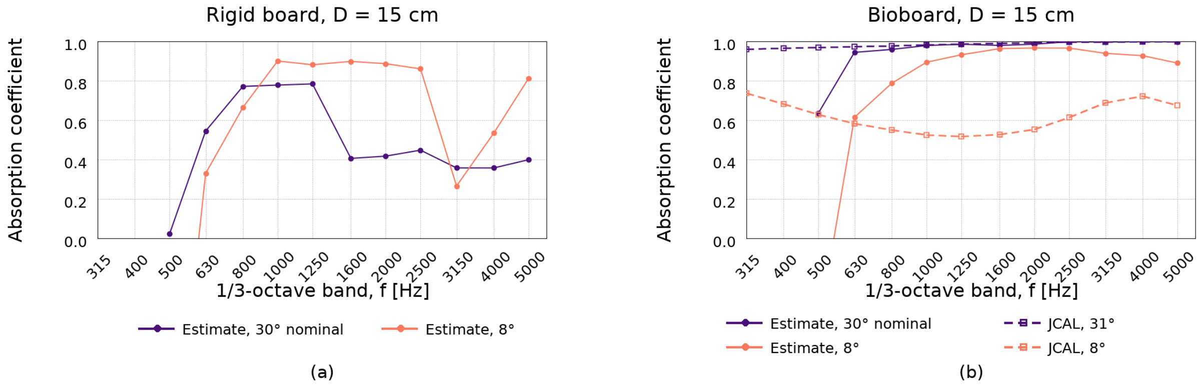

Figure 3: Apparent sound absorption coefficients obtained from Eq. (8) for (a) the rigid board at nominal grazing angles of 30° and 8°, and (b) the bioboard compared with JCAL predictions for a 30-mm layer with an anechoic termination. In panel (b), solid curves denote the boostlet-based estimates and dashed curves denote JCAL values sampled at the displayed third-octave-band centre frequencies; colour identifies the corresponding angle pair. The nominal 30° measurement yielded a wavenumber-derived effective angle of $\beta_{\text{eff}} = 30.68^\circ$ and is therefore compared with the JCAL calculation at $\beta = 31^\circ$, whereas the nominal 8° measurement is compared with the model at $\beta = 8^\circ$.

complete measurement and processing chain rather than as a pointwise validation of the material model. Panel (a) exposes systematic error under a nominally low-absorption boundary condition, whereas panel (b) assesses whether the recovered bioboard trends are compatible with an independent material prediction. Agreement at the high-angle configuration does not eliminate the bias identified using the rigid board, and the discrepancy at 8° cannot be attributed solely to the material model. Moreover, the JCAL benchmark represents a laterally homogeneous equivalent-fluid layer and does not account for edge and corner diffraction from the finite sample.

The finite aperture further restricts the interpretable frequency range. Its wavenumber resolution is approximately $\Delta k = \frac{2\pi}{L_x} = 8.85\ \mathrm{rad\,m^{-1}}$, corresponding to $\Delta f \simeq \frac{c}{L_x \cos\beta} \approx 560$ Hz for the high-angle configuration when using $\beta_{\text{eff}} = 30.68^\circ$. Consequently, the lowest third-octave bands contain too few independent spatial-frequency samples for stable directional separation. Edge and corner diffraction also become more prominent as the sample becomes acoustically small, while the present one-dimensional measurement section cannot capture the complete diffracted field.

5. Conclusion and outlook

Boostlets provide a compact, physics-driven representation of the measured space–time field in the vicinity of the material sample. The tested 1D geometry parallel to the sample does not generally map incident and reflected wavefronts to disjoint coefficient support. For the nominal 30° high-angle configuration ($\beta_{\text{eff}} = 30.68^\circ$), a geometric translation mask gives partial separation and broad qualitative agreement with the $\beta = 31^\circ$ JCAL prediction, while the rigid reference still reveals systematic bias. At 8°, support overlap prevents a reliable absorption estimate and the displayed trend differs from the model. The result is therefore a limit of the complete measurement–representation pair, not evidence that boostlets are intrinsically unable to separate wavefields.

Future experiments should rotate or otherwise reshape the array aperture so that incident, specular, and dominant scattered fronts differ in boost as well as translation. Other tests include increasing L_x to improve low-frequency resolution, and quantifying sensitivity to coefficient threshold and boundary offset. Furthermore, if outgoing specular and scattered contributions can be assigned disjoint supports, their energies may be reported separately and combined consistently when estimating true material absorption.

6. Acknowledgments

This work is part of the Q-Q City project, funded through the Seed Fund Initiative of the European University Alliance Unite!, University Network for Innovation, Technology and Engineering. E.Z. acknowledges the financial support of the Swedish Research Council (Vetenskapsrådet) Grants No. 2020-04668 and 2025-03936.

References

[1] International Organization for Standardization, *Acoustics—determination of acoustic properties in impedance tubes—part 2: Two-microphone technique for normal sound absorption coefficient and normal surface impedance*, Geneva, Switzerland, 2023.

[2] International Organization for Standardization, *Acoustics—measurement of sound absorption in a reverberation room*, Geneva, Switzerland, 2003.

[3] M. Tamura, "Spatial fourier transform method of measuring reflection coefficients at oblique incidence. i: Theory and numerical examples," *The Journal of the Acoustical Society of America*,

vol. 88, no. 5, pp. 2259–2264, 1990. DOI: 10.1121/1.400068.

[4] M. Tamura, J. F. Allard, and D. Lafarge, "Spatial fourier-transform method for measuring reflection coefficients at oblique incidence. ii: Experimental results," *The Journal of the Acoustical Society of America*, vol. 97, no. 4, pp. 2255–2262, 1995. DOI: 10.1121/1.412940.

[5] E. Brandão, A. Lenzi, and S. Paul, "A review of the in situ impedance and sound absorption measurement techniques," *Acta Acustica united with Acustica*, vol. 101, no. 3, pp. 443–463, 2015. DOI: 10.3813/AAA.918840.

[6] A. Richard, E. Fernandez-Grande, J. Brunskog, and C.-H. Jeong, "Estimation of surface impedance at oblique incidence based on sparse array processing," *The Journal of the Acoustical Society of America*, vol. 141, no. 6, pp. 4115–4125, 2017. DOI: 10.1121/1.4983756.

[7] J. Hald, W. Song, K. Haddad, C.-H. Jeong, and A. Richard, "In-situ impedance and absorption coefficient measurements using a double-layer microphone array," *Applied Acoustics*, vol. 143, pp. 74–83, 2019. DOI: 10.1016/j.apacoust.2018.08.027.

[8] M. Nolan, "Estimation of angle-dependent absorption coefficients from spatially distributed in situ measurements," *The Journal of the Acoustical Society of America*, vol. 147, no. 2, EL119–EL124, 2020. DOI: 10.1121/10.0000716.

[9] M. Alkmim, J. Cuenca, L. De Ryck, and W. Desmet, "Angle-dependent sound absorption estimation using a compact microphone array," *The Journal of the Acoustical Society of America*, vol. 150, no. 4, pp. 2388–2400, 2021. DOI: 10.1121/10.0006566.

[10] E. Brandão, A. Lenzi, and J. Cordioli, "Estimation and minimization of errors caused by sample size effect in the measurement of the normal absorption coefficient of a locally reactive surface," *Applied Acoustics*, vol. 73, no. 6–7, pp. 543–556, 2012. DOI: 10.1016/j.apacoust.2011.09.010.

[11] M. Ottink, J. Brunskog, C.-H. Jeong, E. Fernandez-Grande, P. Trojgaard, and E. Tiana-Roig, "In situ measurements of the oblique incidence sound absorption coefficient for finite sized absorbers," *The Journal of the Acoustical Society of America*, vol. 139, no. 1, pp. 41–52, 2016. DOI: 10.1121/1.4938225.

[12] E. Zea, M. Laudato, and J. Andén, "A boostlet transform for wave-based acoustic signal processing in space–time," *Signal Processing*, vol. 244, p. 110 528, 2026. DOI: 10.1016/j.sigpro.2026.110528.

[13] E. Zea, M. Laudato, and J. Andén, "Sparse wavefield reconstruction and denoising with boostlets," in *Proc. International Conference on Sampling Theory and Applications (SampTA)*, 2025. DOI: 10.1109/SampTA64769.2025.11133531.

[14] T. Iwase, Y. Izumi, and R. Kawabata, "A new measuring method for sound propagation constant by using sound tube without any air spaces back of a test material," in *INTER-NOISE and NOISE-CON congress and conference proceedings*, Institute of Noise Control Engineering, vol. 1998, 1998, pp. 1265–1268.

[15] International Organization for Standardization, *ISO 9053-1:2018 - Acoustics-Determination of airflow resistance-Part 1: Static airflow method*, Standard, Geneva, Switzerland, 2018.

[16] Matelys Research Lab, *Rokcell*, https://rokcell.matelys.com/, Accessed 5 May 2026.

[17] Matelys Research Lab, *Alphacell*, https://alphacell.matelys.com/, Accessed 5 May 2026.

[18] A. Beck and M. Teboulle, "A fast iterative shrinkage-thresholding algorithm for linear inverse problems," *SIAM Journal on Imaging Sciences*, vol. 2, no. 1, pp. 183–202, 2009. DOI: 10.1137/080716542.